Quantification and mitigation of PIV bias errors caused by intermittent particle seeding and particle lag by means of large eddy simulations

OPEN ACCESS
IOP Publishing
Measurement Science and Technology
Meas. Sci. Technol. **32** (2021) 104006 (18pp)
https://doi.org/10.1088/1361-6501/ac07d9

Quantification and mitigation of PIV bias errors caused by intermittent particle seeding and particle lag by means of large eddy simulations

Fabio J W A Martins[1,*], **Jonas Kirchmann**[2], **Andreas Kronenburg**[2] and **Frank Beyrau**[1]

[1] Institute of Fluid Dynamics and Thermodynamics, Otto von Guericke University Magdeburg, Magdeburg, Germany
[2] Institute for Combustion Technology, University of Stuttgart, Stuttgart, Germany

E-mail: fabio.martins@ovgu.de

Received 27 November 2020, revised 21 May 2021
Accepted for publication 3 June 2021
Published 21 June 2021

Abstract

In the present work, a standard large eddy simulation is combined with tracer particle seeding simulations to investigate the different PIV bias errors introduced by intermittent particle seeding and particle lag. The intermittency effect is caused by evaluating the velocity from tracer particles with inertia in a region where streams mix with different seeding densities. This effect, which is different from the vastly-discussed particle lag, is frequently observed in the literature but scarcely addressed. Here, bias errors in the velocity are analysed in the framework of a turbulent annular gaseous jet weakly confined by low-momentum co-flowing streams. The errors are computed between the gaseous flow velocity, obtained directly from the simulation, and the velocities estimated from synthetic PIV evaluations. Tracer particles with diameters of 0.037, 0.37 and 3.7 μm are introduced into the simulated flow through the jet only, intermediate co-flowing stream only and through both regions. Results quantify the influence of intermittency in the time-averaged velocities and Reynolds stresses when only one of the streams is seeded, even when tracers fulfil the Stokes-number criterion. Additionally, the present work proposes assessing unbiased velocity statistics from large eddy simulations, after validation of biased seeded simulations with biased PIV measurements. The approach can potentially be applied to a variety of flows and geometries, mitigating the bias errors.

Keywords: bias error, PIV error, particle lag, velocity slip, intermittent seeding, uncertainty

(Some figures may appear in colour only in the online journal)

1. Introduction

Particle image velocimetry (PIV) is a well established optical measurement technique for fluid flow diagnostics (Raffel *et al* 2018, Scharnowski and Kähler 2020). The general principle of a dual-frame single-exposure planar PIV (Adrian 1991, Willert and Gharib 1991) is briefly described as follows. First, the flow is seeded with tracer particles and it is shortly twice illuminated by a light sheet. The light scattered by the particles from each illumination is recorded by a camera in different image frames. Then, the particle image pair is divided into small windows (called interrogation windows), and the local displacement of the particle pattern inside each window is evaluated based on the cross-correlation of the window pair. Afterwards, the image displacement is converted into a physical

* Author to whom any correspondence should be addressed.

displacement using a calibration. Finally, the flow velocity in each window pair is calculated dividing the computed displacement by the known time interval between the two illuminations. The evaluation is repeated for all windows in the particle image pair, producing a 2-component 2-dimension velocity field.

One key aspect of the PIV measurement is the tracer particle seeding because the technique relies on the indirect determination of the fluid motion by the displacement evaluation of tracer particle patterns. Therefore, the adopted particles need to faithfully follow the local fluid motion (without disturbing the flow and the fluid properties) and the image seeding density should be uniform, at least to some extent, in order to provide reliable measurements within the desired accuracy (Melling 1997, Raffel *et al* 2018, Scharnowski and Kähler 2020).

The discrepancies between fluid and tracer particle motion, sometimes called 'particle lag' or 'velocity slip', are mainly influenced by inertial, thermophoretic (combustion) and Brownian (micro-flow) forces (Sung *et al* 1994, Stella *et al* 2001, Raffel *et al* 2018). The selection of suitable tracers in practical situations can be achieved based on the Stokes number (or a modified version of this number taking into account other than inertial effects), which compares the particle response time (related to the particle size and to the difference between particle and fluid densities) with the characteristic time scale of the flow. These issues have already thoroughly been discussed by many researchers (e.g. Samimy and Lele 1991, Melling 1997, Stella *et al* 2001, Bergthorson and Dimotakis 2006, Picano *et al* 2011, Ragni *et al* 2011, Williams *et al* 2015) and the reader is referred to these references for further detail.

Nevertheless, even when errors in the velocity measurement due to the particle lag can be neglected with respect to the other sources of error, the undesired temporal and spatial inhomogeneity of the image seeding density can result in very few tracers inside a specific cross-correlation window, degrading a reliable evaluation of the local motion behaviour of this fluid region. That includes not only a potential error in the detection of the correct cross-correlation peak (because signal-to-noise ratio decreases with image seeding density), but also a bias error in the fluid motion towards the motion of these few tracers because random sampling of flow velocity will not be achieved.

Within this work the focus will be on this problem, which is termed as 'intermittent particle seeding' (elsewhere sometimes called 'conditional particle sampling'). The problem can arise from an integrated effect of the particle lag (also for particles with insignificant inertia), in the case of strong vortices (Stanislas *et al* 2003), vicinity of wall regions (Kähler *et al* 2012), turbomachinery flows (Wernet 2000), shocks in supersonic flows (Ragni *et al* 2011) or flame fronts in combustion (Battista *et al* 2011), to mention just few examples. The inhomogeneity in the seeding concentration can also be a result of the selective seeding of parts of the flow (Melling 1997) due to experimental constrains, for instance, seeded turbulent jets issuing into an unseeded ambient (Rice *et al* 2015, Martins *et al* 2020). In this case, as explained by Samimy and Wernet (2000), since only the high-momentum jet is seeded and the PIV measurements are computed based on tracer particles, then conditional sampling will appear. This happens because, if particles carried by a coherent structure that originated in the jet stream are located in the mixing region at the time of measurement, the velocities associated with that structure will be taken into account. On the other hand, if a coherent structure that was originated from the outer jet region with low momentum is located in the mixing region at the moment of the measurement, the velocities associated with that structure will not be accounted for in the PIV evaluation because the structure does not contain tracer particles. The velocity values from the latter coherent structure most probably are lower and less dynamic than those from the jet. Therefore, the computed statistics will be biased toward the characteristics of the high-momentum seeded jet.

Generally, the statistical results are biased toward the stream most seeded in the occurrence of inhomogeneous seeding concentration (Dibble *et al* 1987), which can increase the systematic uncertainty in the PIV measurements (Sciacchitano 2019). Particularly, the intermittent bias error is pronounced with the velocity difference between seeded and unseeded streams in the mixing region (Rice *et al* 2015). It is important to emphasize that the aforementioned errors due to intermittent sampling are not restricted to PIV, but also affect other seeding-based techniques (Samimy and Wernet 2000, Li *et al* 2007), such as laser Doppler velocimetry (McLaughlin and Tiederman 1973, Birch and Dodson 1980, Dibble *et al* 1987, Fuchs *et al* 1994, Nobach 2015), Doppler global velocimetry (Smith 1998, Thurow *et al* 2008) and particle tracking velocimetry (Li *et al* 2012). Although the intermittency in the particle seeding has been extensively observed, quantitative studies about its consequences in the PIV measurements are hardly found in the literature (Kähler *et al* 2012, Rice *et al* 2015).

The objective of the present work is, therefore, to investigate the potential bias error in PIV measurement statistics introduced by locally intermittent particle seeding and particle lag. Unbiased statistics can be assessed from large eddy simulation computations after matching biased seeded simulations with measurements. The approach, which can be potentially applied to a variety of flows and geometries, is demonstrated in a turbulent annular gaseous jet issued from the nozzle of a standard burner (SpraySyn burner) into low-momentum co-flowing streams under non-combusting conditions (isothermal flow) (Schneider *et al* 2019, Martins *et al* 2020). To this end, seeded large eddy simulations are performed to generate synthetic PIV fields. Nine seeding scenarios are investigated, including three different tracer particle diameters with selective flow seeding through the jet only, the intermediate co-flowing stream only and through both regions.

The chosen SpraySyn burner is motivated by the validation necessity of simulated flows under non-combusting (focus of the present work) and combusting conditions through the burner using possibly biased PIV measurements due to selective seeding of the jet only (Martins *et al* 2020). The low porosity of the sintered matrix of this burner (SpraySyn serial number SSB- 2018-12) precludes seeding the co-flowing streams

(Martins *et al* 2020). The PIV technique is employed due to its capability to additionally work under hostile environments of combusting flows, where most velocimetry techniques fail. The burner is a recently-developed standard lab-scale device for systematic investigations of particle formation from flame spray pyrolysis (Schneider *et al* 2019). This process has the potential to produce countless functional materials with tunable characteristics (Strobel and Pratsinis 2007, Schulz *et al* 2018). Nevertheless, a better understanding of prevailing physical-chemical mechanisms linked to the particle formation is still needed (Schulz *et al* 2018). The knowledge is ultimately acquired from experiments and validated simulations. The best available flow field statistics can help to understand the particle formation processes in the burner and hence this work quantifies and mitigate possible bias errors in the measured velocity statistics due to intermittent particle seeding and particle lag. We discuss the applicability and limitations of assessing unbiased statistics from biased numerical simulations that mimic the physics responsible for the bias effect on the measurements.

2. Theoretical background

One of the critical sources of error in the velocity measurements by PIV is the particle response time. The motion of spherical tracer particles seeded in a viscous fluid described in the work of Sung *et al* (1994) can be extended to account for Brownian effects (Santiago *et al* 1998). The resulting governing equation of the general particle motion is given by

$$\mathbf{F}_{\mathrm{PI}} = \mathbf{F}_{\mathrm{SV}} + \mathbf{F}_{\mathrm{PG}} + \mathbf{F}_{\mathrm{FI}} + \mathbf{F}_{\mathrm{FU}} + \mathbf{F}_{T} + \mathbf{F}_{G} + \mathbf{F}_{C} + \mathbf{F}_{E} + \mathbf{S}_{\mathrm{RD}}\,, \tag{1}$$

where the particle inertial force $\mathbf{F}_{\mathrm{PI}}$ is balanced by the Stokes viscous force $\mathbf{F}_{\mathrm{SV}}$, the pressure gradient force on the fluid $\mathbf{F}_{\mathrm{PG}}$, the fluid inertial force $\mathbf{F}_{\mathrm{FI}}$, the unsteady fluid force $\mathbf{F}_{\mathrm{FU}}$, the thermophoretic force $\mathbf{F}_{T}$, the gravitational force $\mathbf{F}_{G}$, the centrifugal force $\mathbf{F}_{C}$, the electrostatic force $\mathbf{F}_{E}$ and a random source $\mathbf{S}_{\mathrm{RD}}$ related to Brownian effects. The equation neglects collision against walls and between particles, due to the commonly low particle concentration in PIV (Raffel *et al* 2018).

The above equation can be considerably simplified when solid tracer particles are employed in gas-phase flows (fluid density much lower than that of commonly-used particles) under isothermal (without fluid density change) and macroscopic conditions. In this case, following Raffel *et al* (2018), the particle inertial force is equilibrated by only the Stokes viscous force according to the approximation

$$\frac{\rho_p \pi d_p^3}{6}\frac{d}{dt}\mathbf{V}_p = -3\pi\mu d_p\left[\mathbf{V}_p - \mathbf{V}_f\right], \tag{2}$$

where d_p is the particle diameter, ρ_p is the particle density, μ is the fluid viscosity, $\mathbf{V}_p$ is the particle velocity, $\mathbf{V}_f$ is the velocity of the surrounding fluid and $[\mathbf{V}_p - \mathbf{V}_f]$ is the velocity slip.

The step response of a tracer particle to a sudden acceleration of surrounding fluid assumes the well-known exponential solution

$$\mathbf{V}_p = \mathbf{V}_f\left[1 - e^{-\frac{t}{\tau_p}}\right], \tag{3}$$

where τ_p stands for the particle relaxation time (sometimes called particle response time)

$$\tau_p = \frac{\rho_p}{18\mu} d_p^2. \tag{4}$$

For sub-micron tracer particles, the no-slip boundary condition assumption may fail. Therefore, corrections for the Stokes viscous force (and consequently for the relaxation time) have been proposed based on the Knudsen number (e.g. Sung *et al* 1994), defined as the ratio between the mean free path of the fluid and the particle diameter.

To estimate the tracer particle tendency to follow the surrounding fluid flow, the Stokes number can be employed. It is defined as the ratio of the relaxation time of the tracer particle to a characteristic time of the flow

$$\mathrm{St} \equiv \frac{\tau_p}{\tau_f}, \tag{5}$$

where the characteristic time scale of the flow τ_f is often inferred as a ratio of a representative length scale and a characteristic velocity (Raffel *et al* 2018). Ideally, St should be much lower than 1, but the scattered light from tracer particles also depends on their diameter, therefore $\mathrm{St} < 0.1$ is normally considered as good practice (Raffel *et al* 2018). For St below 0.2, tracer particles are expected to closely track the flow velocity gradients, with velocity slip errors below 2% (Samimy and Lele 1991).

Usually, the characteristic time scale of the flow is assumed to be the turnover time of large eddy structures (τ_{ℓ_0}) defined as

$$\tau_f = \tau_{\ell_0} \equiv \frac{\ell_0}{V_{\ell_0}}, \tag{6}$$

where ℓ_0 and V_{ℓ_0} are the characteristic lengthscale and the characteristic velocity of a large eddy, respectively.

For the present investigated turbulent jet flow, a characteristic time of the flow at a few diameters downstream the jet exit is crudely estimated assuming a characteristic lengthscale equal to the jet nozzle outer diameter D_0 and a characteristic velocity equal to the jet bulk velocity V_0. This characteristic time is a reasonable scale for providing meaningful time-averaged velocity and Reynolds stress measurements, since the characteristic velocity is of the order of $(2K/3)^{1/2}$, being K the turbulence kinetic energy, for fully turbulent flows at high Reynolds number (Pope 2000). At the vicinity of the annular nozzle exit, an inner mixing region with strong flow recirculation is formed (Ko and Chan 1979). At this region, the characteristic lengthscale of the flow is then proportional to the slit of the annular nozzle, leading to the smallest characteristic time of the annular jet flow. For downstream positions, the characteristic time of the flow increases since $\tau_f \propto R_{0.5}/V_c \propto z^2/(V_0 D_0)$, being V_c the centreline velocity, $R_{0.5}$ the half-velocity width (radial position where the $V_z = 0.5\,V_c$) and z the axial position from the jet exit (Pope 2000). Nevertheless, if high-accuracy of the smallest scale fluctuations is important

(e.g. dissipation measurements), the Kolmogorov time scale should be used instead, which is defined as

$$\tau_\eta \equiv \left[\frac{\nu}{\epsilon}\right]^{1/2}, \tag{7}$$

where ν is the kinematic viscosity of the fluid and ε is the dissipation rate of turbulence kinetic energy by viscous stresses.

Besides the ability of the particle tracer to track the fluid flow, it is worth mentioning that the instantaneous velocity measured by PIV, $\mathbf{V}_{\mathrm{PIV}}$, is the volume average of the fluid element velocity (estimated by the tracer particles) over the interrogation box region $\forall$, which can be expressed by the following equation (Atkinson *et al* 2014)

$$\mathbf{V}_{\mathrm{PIV}} \approx \int \omega \mathbf{V}_f d\forall \approx \int \omega \mathbf{V}_p \, d\forall, \tag{8}$$

where ω, to a first approximation, can be obtained by a top-hat weighting function representing the interrogation box region according to

$$\omega = \frac{1}{\Delta W_x \Delta W_y \Delta W_z \Delta t}, \tag{9}$$

where $\Delta \mathrm{W}_x$ and $\Delta \mathrm{W}_y$ are the dimensions of the interrogation window, $\Delta \mathrm{W}_z$ the light sheet thickness and Δt the time delay between light pulses. Therefore, the interrogation box region acts as a low-pass filter of the spatial and temporal gradients of the local velocity. This can cause relevant bias errors in the velocity statistics, particularly for the higher-order moments of the turbulent velocity fluctuations (Atkinson *et al* 2014). The best-practice PIV experimental design for fine spatial resolution and accurate higher-order statistics in turbulent flows should optimize the interrogation box dimensions so as to resolve small-scale motions of about a few Kolmogorov length scales (Elsinga and Marusic 2010), with the latter being defined as

$$\eta \equiv \left[\frac{\nu^3}{\epsilon}\right]^{1/4}. \tag{10}$$

A thorough discussion about the spatial filtering effects in the PIV measurements can be found elsewhere (Foucaut *et al* 2004, Atkinson *et al* 2014).

It should be clear from the above discussion that the measured PIV velocity intrinsically carries errors from various sources. Therefore, the measured velocity must always include its uncertainty, characterizing the statistical dispersion of the values that reasonably resembles the 'true' flow velocity (GUM 2008). The standard uncertainty in the local velocity of the time-averaged PIV fields, δV_i, can be estimated as (GUM 2008, Sciacchitano 2019)

$$\delta V_i = \sqrt{{\delta V_{i,A}}^2 + {\delta V_{i,B}}^2} = \sqrt{\left[\frac{\sigma_{V_i}}{\sqrt{N_{\mathrm{eff}}}}\right]^2 + {\delta V_{i,B}}^2}, \tag{11}$$

where $\delta V_{i,A}$ and $\delta V_{i,B}$ stand for type-A and type-B uncertainties, respectively, of the ith component of the time-averaged velocity vector, σ_{V_i} is the standard deviation and N_{eff} is the local effective number of vectors (i.e. time-independent samples). N_{eff} can be estimated based on the integral time scale as (Sciacchitano and Wieneke 2016)

$$N_{\mathrm{eff}} = \frac{N}{\sum\limits_n \rho_{V_i V_i}(n\Delta t)}, \tag{12}$$

where N is the amount of samples, $\rho_{V_i V_i}$ is the auto-correlation coefficient, n is the time lag and Δt is the sampling interval. The auto-correlation coefficient equals one for $n = 0$ and decreases towards zero with increasing n. Note that, for uncorrelated samples, $\rho_{V_i V_i}(n\Delta t) = 0$ when $n > 0$ leading to $\sum \rho_{V_i V_i}(n\Delta t) = 1$ and consequently $N_{\mathrm{eff}} = N$, whereas, for correlated samples, $\sum \rho_{V_i V_i}(n\Delta t) > 1$ resulting in $N_{\mathrm{eff}} < N$.

The type-A uncertainty represents the random uncertainty due to the finite number of samples. It includes the random uncertainty of the instantaneous measurements as well as the velocity fluctuations due to the stochastic nature of the flow (Sciacchitano and Wieneke 2016). The type-B uncertainty is evaluated by means other than the statistical analysis of series of samples, usually using available knowledge, and includes possible bias in the measurements. In practice, the type-B uncertainties are generally neglected (Sciacchitano and Wieneke 2016), but they can be estimated by comparing the PIV measurements to analytical solutions, reliable simulations or high-accuracy measurements preferably from a different technique. The estimation of the type-B uncertainty provides a more realistic standard uncertainty, because a lower bound (related to the best accuracy of the measurement technique) exists when the amount of independent samples tends to infinity. In the present work, $\delta V_{i,B} \approx 0.02$ pixel is assumed based on the root-mean-square error of synthetic PIV fields with constant displacement under optimum conditions (i.e. particle image diameter of about 3 pixels, 5–15 particles per interrogation window, no particle pair loss, no shear, no noise) (Thielicke and Stamhuis 2014).

The standard uncertainty in the adimensional velocity, $\delta\left(V_i/V_c\right)$, employed in radial self-similar profiles, is computed by uncertainty propagation (GUM 2008, Sciacchitano 2019) according to

$$\begin{aligned}\delta\frac{V_i}{V_c} &= \sqrt{\left[\frac{\partial}{\partial V_i}\left(\frac{V_i}{V_c}\right)\delta V_i\right]^2 + \left[\frac{\partial}{\partial V_c}\left(\frac{V_i}{V_c}\right)\delta V_c\right]^2} \\ &= \sqrt{\left[\frac{1}{V_c}\delta V_i\right]^2 + \left[\frac{V_i}{V_c^2}\delta V_c\right]^2},\end{aligned} \tag{13}$$

where δV_c is the standard uncertainty in the centreline velocity.

The standard uncertainty in the Reynolds stress, δR_{ij}, can be estimated as (Sciacchitano and Wieneke 2016)

$$\delta R_{ij} = \sqrt{\left[\sigma_{V_i}\sigma_{V_j}\sqrt{\frac{1+\rho_{V_iV_j}^2}{N_{eff}-1}}\right]^2 + \left[\rho_{\delta V_{i,B}\delta V_{j,B}}\delta V_{i,B}\delta V_{j,B}\right]^2}, \tag{14}$$

where $\rho_{V_iV_j}$ refers to the cross-correlation coefficient between the velocity components V_i and V_j $(-1 \leqslant \rho_{V_iV_j} \leqslant 1)$ and

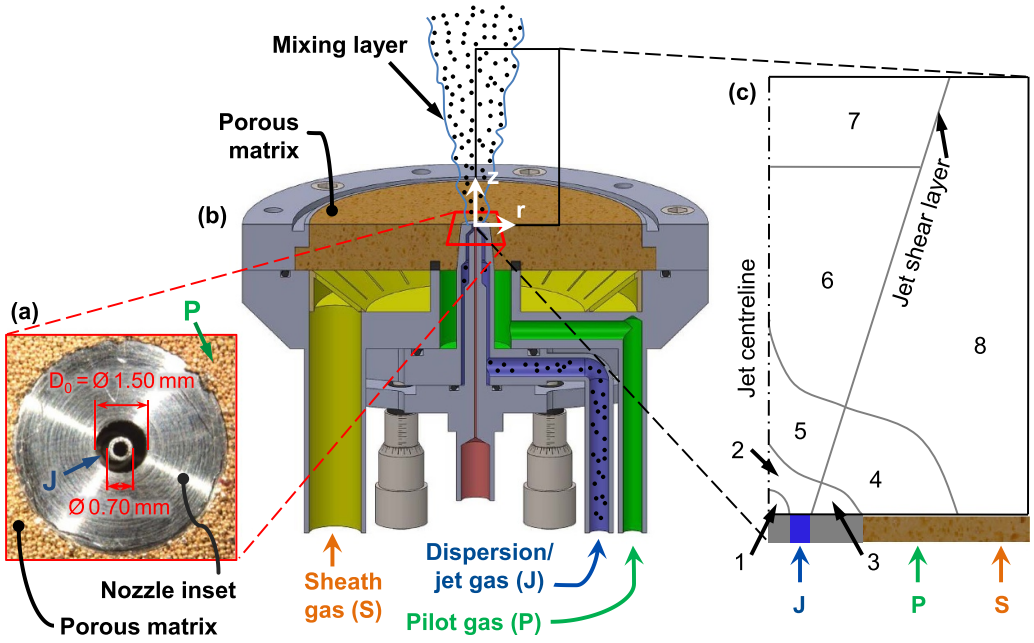

Figure 1. (a) Top view picture of the nozzle outlet with dimensions, (b) schematic cross-sectional view of the SpraySyn-burner with an example of selective particle seeding through the dispersion gas for PIV evaluation, and (c) characteristic regions of the flow field. Legend: (1) inner mixing region, (2) jet merging region, (3) annular mixing region, (4) pilot merging region, (5) jet-pilot mixing region, (6) fully-merged jet, (7) developed jet and (8) sheath region. (For interpretation of the colour in this figure, the reader is referred to the web version of this article).

$\rho_{\delta V_{i,B}\delta V_{j,B}}$ is the cross-correlation coefficient between the type-B uncertainty components. The $\rho_{V_iV_j}$ coefficient is equal to one for the Reynolds normal stresses and it is zero when the velocity components are uncorrelated. Generally, the type-B uncertainty components are uncorrelated for planar PIV ($\rho_{\delta V_{i,B}\delta V_{j,B}} = 0$) (Sciacchitano and Wieneke 2016).

The expanded uncertainties are computed multiplying the standard uncertainties by a coverage factor, λ, associated with a confidence level and the local amount of independent samples. The coverage factor is obtained from the t-student distribution (GUM 2008). The reported uncertainties in the present work refer to the expanded uncertainties with a confidence level of 95% (i.e. $\lambda = 1.96$ for $N_{\text{eff}} \gtrsim 500$).

3. SpraySyn burner and flow regions

The SpraySyn burner (figure 1) is a standard lab-scale spray-flame burner for systematic experimental, numerical and analytical investigations of nanoparticle synthesis (Menser *et al* 2014, Schneider *et al* 2019). In the standard operation of the SpraySyn burner, a central two-fluid nozzle atomizes a liquid solution of precursor-solvent mixture by a high-momentum dispersion gas of oxygen. The liquid is delivered through a capillary at the center of the nozzle (red region in figure 1), while dispersion gas (blue) flows through an annular region with inner diameter of 0.70 mm and outer diameter of $D_0 = 1.50$ mm. The flow is stabilized by a surrounding laminar premixed flat fame from the reaction of a methane-oxygen pilot gas (green) supported on a porous sintered matrix with an outer diameter of 70 mm. A laminar coflow of nitrogen in the outermost annular region is employed as an inert sheath gas (yellow). The flow statistics are axisymmetric. More details about the SpraySyn burner can be found in the works of Schneider *et al* (2019) and Martins *et al* (2020).

In the present work, we simulate a non-reacting flow with gas flow rates of 4 slm of dispersion gas (also termed jet gas), 7.5 slm of pilot gas, 120 slm of sheath gas, without any injection of precursor, under 1 atm and 293 K (identical to case 1 measured by Martins *et al* 2020). This leads to outlet bulk velocities of 51.8 m s^{-1}, 1.1 m s^{-1} and 0.6 m s^{-1} for the jet, pilot and sheath gases, respectively.

The investigated flow field issued through the SpraySyn burner can be defined as a non-reacting, axisymmetric, turbulent annular jet weakly confined by co-flowing low-momentum streams (the ratio between pilot and jet velocities is around 0.02). The flow can be divided along the jet centreline sequentially into merging zones, fully-merged zone, and fully-developed zone, combining previous works in the literature (Ko and Kwan 1976, Ko and Chan 1979, Martins *et al* 2020). The inset on the right of figure 1 presents a sketch with subdivisions of the flow field that will help discussing the results. It is important to stress that the divisions are meant to define regions with similar relevant characteristics, which might persist in other regions. Therefore, the border limits separating different regions must be understood as approximated locations. Close to the nozzle exit, the high-momentum annular jet flow is characterized by a merging region. Within this region, the axis of the jet potential core (region with negligible variation in the initial velocity) merges towards the jet centreline. Due to the absence of a central issuing stream, an inner mixing region is formed with strong presence of vortices, including a toroidal-like recirculation zone close to $z = 0$. The

low-momentum pilot stream issuing through the porous matrix also merges towards the jet centreline. Along the path, the pilot stream encounters the main jet stream and then a vigorous mixing occurs, characterizing the jet-pilot mixing region. The presence of an outer annular wall at the nozzle inset generates an annular mixing region with intense flow recirculation, mostly composed by pilot gas. The combined jet evolves into a fully-merged jet region (with complete merging of the jet and pilot streams) and then into a developed jet region further downstream. From the fully merged zone onwards, the maximum axial time-averaged velocity is observed on the jet centreline and its value decays with the axial and radial directions. In the fully-developed zone, the combined jet exhibit self-similar characteristics (Pope 2000) and behaviour equivalent of that of a turbulent round jet (Ko and Kwan 1976, Martins *et al* 2020). At the rim of the combined jet, a shear layer exists, promoting mixing between the combined jet stream and the surrounding sheath gas.

4. Numerical setup and processing

The numerical simulation is based on the open-source libraries of OpenFOAM-5.x (Weller *et al* 1998). The gaseous flow field and the discrete seeding particles evolve within a cylindrical domain with a diameter of $36\,D_0$ and an axial extent of $20\,D_0$ starting at the burner nozzle exit. The inlet flow rates of the jet, pilot and sheath regions used in the simulation have been described above (section 3). The solution of the gaseous flow field, the discrete seeding particles, the data collection, the synthetic PIV and the processing approach are described in the following.

4.1. Eulerian solver for the gas-phase flow field

The gaseous flow field is obtained by the solution of the incompressible conservation equations of mass and momentum in the context of large eddy simulation (LES). The cylindrical simulation domain is discretized by a multiblock structure. Around the centreline a Cartesian grid is used to avoid singularities, while the remaining domain is resolved by a cylindrical grid. In total the domain is discretized by 1.7 million grid cells, where mesh refinement is applied in the region close to the jet exit to resolve the shear layers (leading to a minimum cell size of $0.0053\,D_0$ in the shear layer on the jet exit plane). The cell size is typically around $5\,\eta$, allowing the cell to resolve 80% of the turbulent kinetic energy on average, except in the vicinity of the jet exit nozzle lip. The remaining turbulent subgrid fluctuations are modelled with the σ-model (Nicoud *et al* 2011) using a constant $C_\sigma = 1.5$.

The turbulent velocity field at the jet inlet boundary is generated in a separate, independent LES, because no velocity measurements were available at the close vicinity of the nozzle exit. The independent LES resolves an annular pipe flow with the same inner and outer diameter as the jet nozzle on the exit plane. In this simulation, the velocity fields are sampled each time step on the nozzle exit plane and imposed at the jet inlet boundary in the subsequent simulation of the SpraySyn burner. Aside from the jet inlet, constant block velocity profiles are applied at the pilot and sheath gas inlets. All remaining boundary conditions are set as zero gradient, except for the pressure at the outlet where a total pressure is imposed.

A second-order central-difference scheme is used for the velocity computation, with a constant time step of 0.2 µs, which ensures Courant numbers below 0.9 at all times. At the end of each time step, a maximum final residual of 1×10^{-10} is allowed for all fields.

4.2. Lagrangian solver for the seeding particles

A Lagrangian point approach is used to track the dispersion of six separate and independent sets of seeding particles, which are evolved by drag and gravitational forces. Potential interactions among particles, shear-induced particle rotation and alterations of the gaseous flow field by the seeding are assumed to be small and neglected. The six sets of particles have two distinct origins, three are injected through the jet inlet (at random locations on the inlet surface of the simulation domain) and the other three through the pilot inlet. The inlet sheath gas is always unseeded. Each of the three sets injected at one inlet has a constant particle density of 3.9 g cm^{-3} and constant particle diameters of 0.037, 0.37 and 3.7 µm. The particles will sometimes be referred along the text as 'small', 'medium' and 'large' particles, in allusion to their diameters. The medium-sized tracer particles are expected to simulate the TiO_2 seeds (Kronos 2160) used in previous PIV measurements of our group (Martins *et al* 2020). The particles are injected with a flow rate of 2.0×10^7 particles per second at the jet inlet and 3.8×10^7 particles per second at the pilot inlet. These two flow rates ensure that each particle represents the same mass of fluid. This leads to an average instantaneous particle number in the domain of around 4.6×10^5 particles for the two sets of smaller particles (0.037 and 0.37 µm) originating from the jet (3.1×10^5 for 3.7 µm) and 4.1×10^6 particles in the two sets of smaller particles with origin from the pilot (4.5×10^6 for 3.7 µm). The total particle number varies depending on the origin of the particle injection due to the different jet and pilot mass flow rates as well as the particle size due to the different particle inertia and initial velocities. The particle concentration in the PIV image will be provided in section 4.4, since it depends not only on the particle concentration per volume, but also on the light sheet thickness, the magnification and the image resolution.

The estimated response times a few diameters downstream the jet exit for the small, medium and large-sized particles (equation (4)) are about 0.016, 1.6 and 1600 µs, respectively, leading to Stokes numbers of $\mathrm{St} \approx 0.0006$, 0.06 and 6. It is important to observe that a variation of one order of magnitude in the particle diameter leads to a variation of two orders in the particle response time and, therefore, in the Stokes number ($\mathrm{St} \propto \tau_p \propto d_p^2$). From the Stokes number criterion, the present small and medium-sized particles are expected to follow the flow with fidelity.

Instantaneous tracer particle distributions from the LES for the different particle diameters studied are presented in figure 2. The figure indicates that all investigated particles

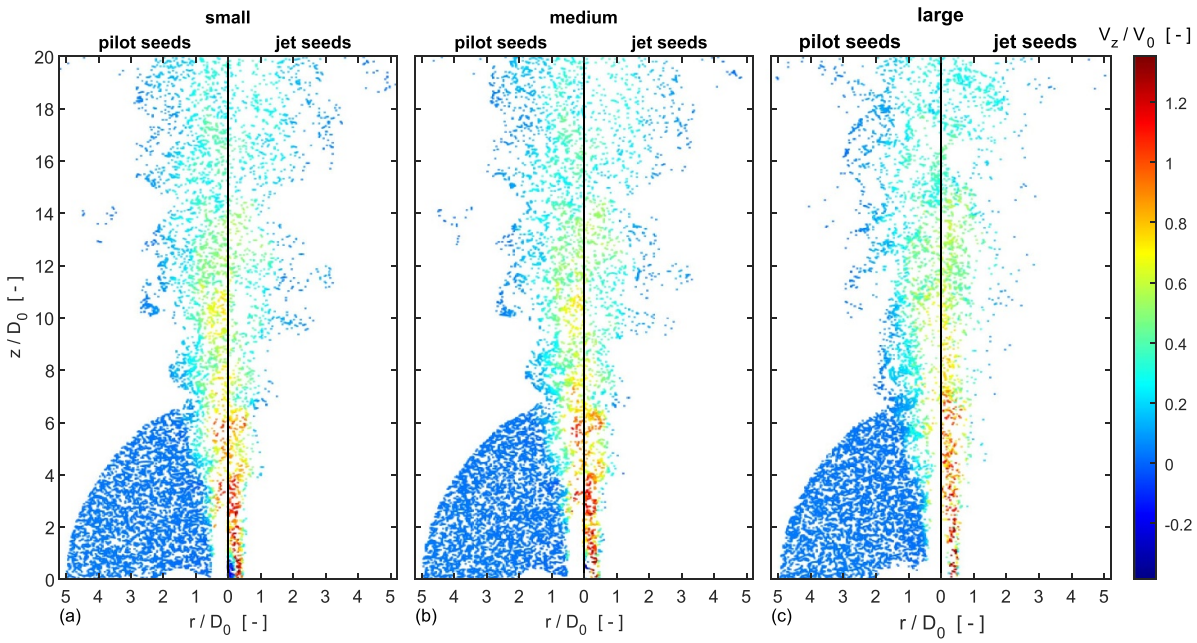

Figure 2. Instantaneous tracer particle distributions from LES for particles with diameters of (a) 0.037, (b) 0.37 and (c) 3.7 μm seeded through the pilot (left half) and jet gas (right half). Particles are coloured according to their axial velocity.

seeded through the pilot gas are sucked towards the high-momentum jet for positions below $6.7\,D_0$ (pilot merging region in figure 1(c)) and follow jet spreading for downstream positions. The spatial distributions for tracer particles with diameters of 0.037 and 0.37 μm are similar with negligible differences from visual inspection of figure 2. All particles sizes injected through the pilot gas (left halves in figure 2) have difficulties to enter in the annular mixing region ($0.5 \lesssim r/D_0 \lesssim 2$ and $z/D_0 \lesssim 0.7$) and jet merging region ($0 \leqslant r/D_0 \lesssim 0.5$ and $z/D_0 \lesssim 2.7$). The former region is dominated by a recirculating flow close to the wall, so only a small amount of particles mixes with the gas while the latter is shielded at some extent by the high-momentum jet flow, particularly the annular jet core close to the nozzle. It is noticeable from the instantaneous plots that there are less particles when the large seeds (with the greatest inertia) are used. The particle number density decreases with axial and radial distances from the nozzle exit, because of the jet dispersion and the radial inflow of surrounding unseeded gas. Nevertheless, the particle number density of small and medium-sized seeds can be considered locally homogeneous inside the most part of the jet and pilot streams. On the other hand, the particle distribution of the large tracers shows inhomogeneities at the jet shear layer with regions of particle clouds and others with a particle shortage. This behaviour is expected from its Stokes number ($\mathrm{St} \gg 0.1$).

4.3. LES data collection and processing

Including the initialization of the flow, the simulation evolved for 150 ms (259 flow through times), which amounts to 12 180 CPUh on two Intel Xeon (E5-2680 v3) processors with a total of 24 cores.

Statistics from the gaseous flow field are computed based on collected data every time step for each LES cell. In total the gaseous flow field is averaged for 120 ms, which corresponds to 208 flow through times based on the jet bulk velocity. The maximal relative change in the averaged Reynolds stresses on the centreline is below 4% within the last third of the averaging period. In addition to the time average, the flow field is averaged along the circumferential direction to improve convergence, exploiting the rotational symmetry of the setup.

Particle positions and their identification numbers of each seeding particle set are recorded every 100th and 120th time step within two $0.27\,D_0$-thick vertical volumes that are orthogonal to each other and centred with diametral jet planes (i.e. *rz*-planes). This leads to a 20 μs sampling period of pairs of particle distributions with a 4 μs time delay between corresponding recordings. The total amount of pairs of instantaneous particle distributions for each simulated set is 3200.

4.4. Synthetic PIV generation and processing

Planar PIV fields of the turbulent jet flow issued through the SpraySyn burner are computed from synthetic particle images using the collected data from the seeded LES in a Monte Carlo basis (Raffel *et al* 2018). For each pair of recorded seeded LES time step, synthetic particle images mimicking a typical dual-frame CCD camera system are generated, according to Raffel *et al* (2018). The centre location of each artificial particle at the first and second image frames (subsequent single-exposure times) is given by its 3D recorded position (x_0, y_0, z_0) at the 100th and 120th LES time step, respectively. In the present work, the image size is 512×1024 pixels along the horizontal and vertical direction, respectively, covering a field of view of $-4.9 \lesssim r/D_0 \lesssim 4.9$ and $0.7 \lesssim z/D_0 < 20$. This leads to a scaling conversion from physical to image space of $0.019\,D_0$/pixel. The maximum particle displacement for the present time delay ($dt = 4$ μs) is about 9 pixels and the loss

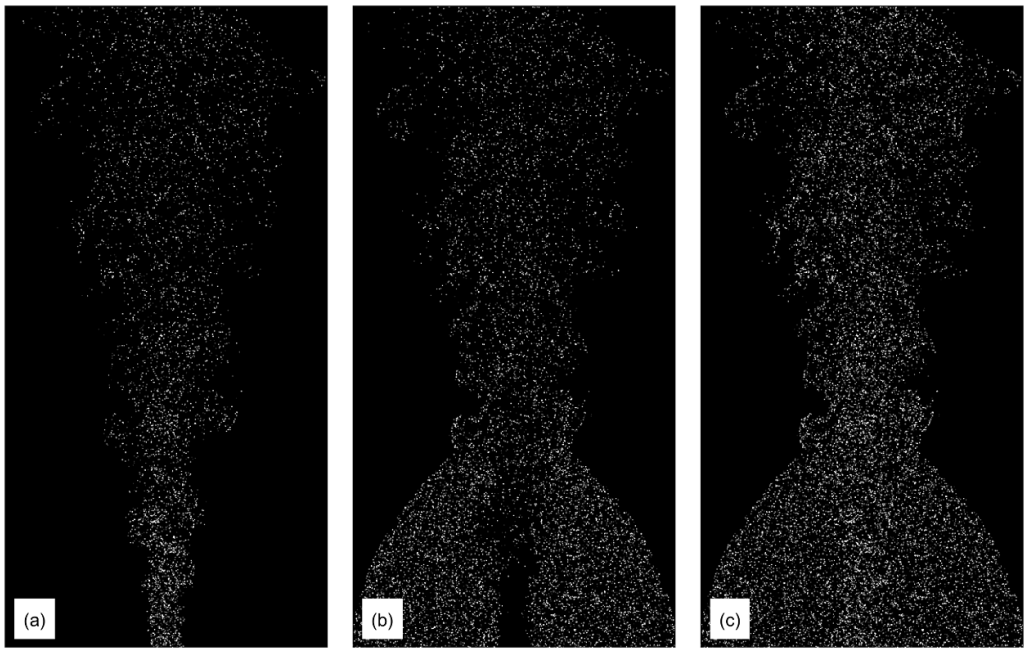

Figure 3. Instantaneous synthetic images of tracer particles for PIV evaluation. Generated seeds through (a) the jet only, (b) the pilot only and (c) both regions.

of corresponding particles is below 3% between subsequent exposures due to out-of-plane motion. The intensity distribution of each particle is approximated by a 2D Gaussian distribution with the standard deviation equal to one quarter of the particle image diameter and the amplitude associated to the depth position of the particle in relation to the centre of the light sheet as follows

$$I(x',y') = I_{z_0}\, e^{-\frac{8}{\delta_\tau^2}\left((x'-x_0')^2+(y'-y_0')^2\right)}, \tag{15}$$

where x' and y' are image coordinates, x_0' and y_0' are converted particle centre locations on the image plane, δ_τ is the particle image diameter and I_{z_0} the maximum intensity of each particle given by

$$I_{z_0} = I_0\, e^{-\frac{8}{\Delta W_z^2} z^2}, \tag{16}$$

where I_0 is the maximum light intensity in the centre of the Gaussian light sheet, ΔW_z is the light sheet thickness and z is the particle depth distance from the centre of the light sheet. In the present work, the image diameter of artificial particles is 2.5 pixels and the light sheet thickness is $0.27\,D_0$. The maximum particle intensity is restricted to 1000 counts in the synthetic 10-bit images generated here. The synthetic images simulate perfect recordings with no image noise or perspective errors, in order to improve the velocity precision. The averaged particle image density in the present setup is around 0.02–0.03 particles per pixel (ppp). Images of the particle distribution from seeds injected simultaneously through the jet and pilot regions are created joining the data collected from particles being added though these distinct regions. Figure 3 presents typical instantaneous synthetic particle images generated by the aforementioned procedure.

The present synthetic PIV processing follows the classical operating rules for planar PIV (Raffel *et al* 2018, Scharnowski and Kähler 2020). The selective seeding method causes spatial inhomogeneity of the image seeding density (figure 3). Therefore, instantaneous masks are used in order to limit the velocity evaluation to regions with tracer particles. The masks are generated by binarizing previously Gaussian-smoothed instantaneous particle images. Velocity fields are computed in PIVlab toolbox for Matlab (Thielicke and Stamhuis 2014, Thielicke 2021) using an iterative multi-grid cross-correlation approach including window deformation (Scarano and Riethmuller 2000). The initial interrogation window size of 64×64 pixels is stepwise decreased along four cross-correlation passes towards the final window size of 16×16 pixels (all windows with 50% of overlap), leading to a final vector space of $0.13\,D_0$ (i.e. about half of the annular slit width of the nozzle). Vectors at grid locations outside the instantaneous mask are not computed. The sub-pixel resolution is obtained by a three-point Gaussian fit of the cross-correlation peak (Raffel *et al* 2018). The interpolation scheme for the window displacement between passes is performed based on the 'Smoothn' algorithm (Garcia 2010). After the final pass, spurious vectors are removed, based on global vector displacement limits and on the local standard deviation of the neighbours (Westerweel and Scarano 2005), and not accounted for computing the statistics. The statistics of each case is calculated using 3200 velocity fields, which are averaged with their mirrored fields with respect to the jet centreline for better convergence. It is important to mention that the local amount of time-independent vectors is much lower than 2×3200 for two reasons. First, the sampling interval of the LES data is not long enough to guarantee completely uncorrelated vectors everywhere, since the jet velocity decreases with axial

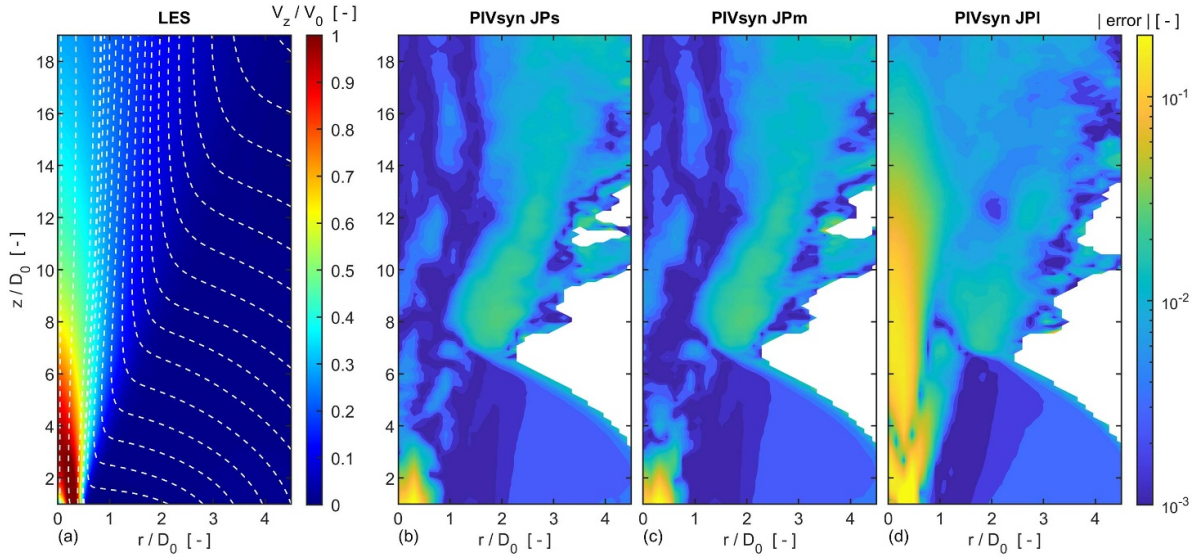

Figure 4. (a) Time-averaged axial velocity field of the gas, with streamlines, computed by large eddy simulation at the PIV region. Absolute error fields between time-averaged axial velocities computed by LES and those evaluated by synthetic PIV using tracer particles of diameters of (b) 0.037 μm, (c) 0.37 μm and (d) 3.7 μm injected through the jet and pilot regions.

and radial directions (increasing the characteristic time scale). Second, the amount of vectors changes locally, due to border oscillation of the seeded jet flow (captured by the instantaneous mask). Therefore, the local effective number of vectors for computing the expanded uncertainties is estimated based on equation (12).

5. Results and discussion

Nine seeding cases are compared and discussed here. The cases consist of simulated tracer particles with diameters of 0.037, 0.37 and 3.7 μm, denoted in the plots by the suffixes 's' (small), 'm' (medium) and 'l' (large), respectively. The particles are injected through the jet gas only (prefix 'J' in the plots), pilot gas only ('P') or both ('JP'). Velocity fields are assessed directly in the standard LES (simulated gaseous flow) and indirectly from PIV evaluation of synthetic images (PIVsyn), i.e. cross-correlation of windows from artificial particle image pairs. The adopted axes are drawn in figure 1. Time-averaged velocity and Reynolds stress statistics are used to discuss the bias errors arising from the use of particles for inferring the gas velocity of the present isothermal turbulent jet.

Figure 4 presents the time-averaged axial velocity field from LES and the absolute error fields from the difference between the LES velocity field non-dimensionalized by the jet bulk velocity and those from synthetic PIV using tracer particles introduced through the jet and dispersion gases together. The comparison of the error fields shows mainly the effect of particle lag on the velocity for the different tracer particle sizes. The colorbar is set in logarithmic scale covering two orders of magnitude of error. White regions are locations where PIV evaluation is not possible due to the lack of tracer particles, because no seeding was added through the sheath gas. Error fields from small and medium particles are alike with few differences in the inner mixing region (please revisit figure 1(c) for flow regions). At this region the characteristic lengthscale of the flow is expected to be of the order of the slit of the annular nozzle (i.e. $0.27\,D_0$), leading to a Stokes number at least four-fold greater than those estimated in section 4. The two plots show negligible errors close to the jet centreline and in the pilot merging region. The errors are higher at the jet shear layer and they are the highest at the annular mixing region. These errors are caused by the presence of large instantaneous velocity gradients (much larger than gradients computed from the time-averaged velocity) and lower particle-number density in these locations. Both effects increase the velocity errors within the corresponding PIV interrogation windows (Raffel *et al* 2018, Sciacchitano 2019). Regarding the large particles, their errors are generally higher than those of the small and medium particles, except for the pilot merging region. The latter region has negligible velocity fluctuations and, therefore, particles of all sizes properly track the flow. The highest errors for the large particles are observed close to the centreline region upstream the developed jet zone and in the annular mixing region. The former is a consequence of the high velocities and fluctuations that preclude the reliable velocity estimations due to the particle inertia. On top of that, at the bottom of the PIV field of view close to the jet exit, the velocity error increases due to the loss of corresponding particles in the PIV interrogation window pair. The origin of such errors and their quantification will be discussed in more detail when presenting the velocity profiles.

Figure 5(a) shows centreline profiles of time-averaged axial velocity obtained from LES and synthetic PIV using tracer particles with different diameters introduced through the jet and pilot gases. For clarity, uncertainty bars are added on every fourth velocity location for the medium-sized particles only. PIV measurements performed by Martins *et al* (2020) are included for comparison. They measured the gaseous

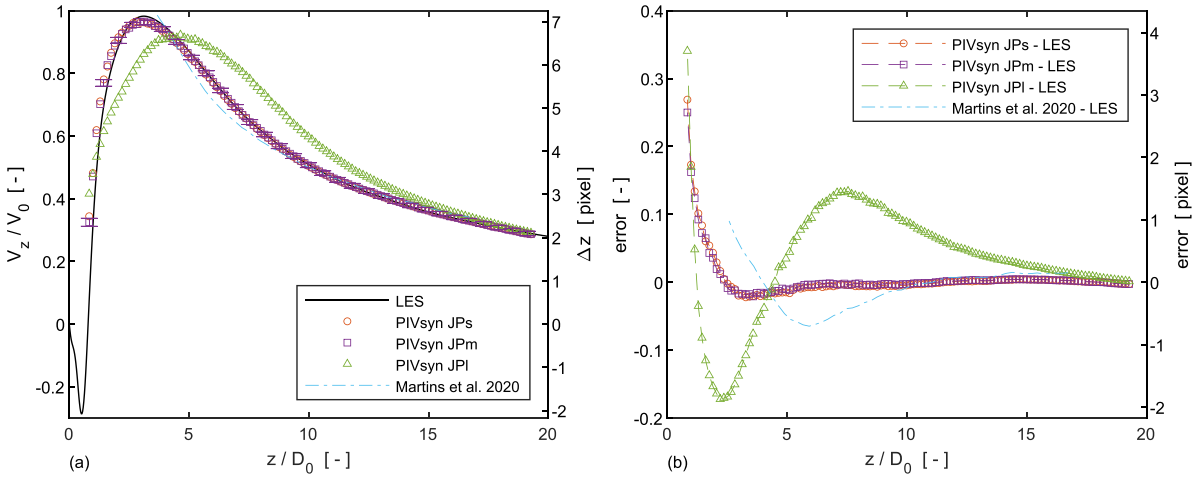

Figure 5. Centreline profiles of (a) time-averaged axial velocity from standard LES, PIV measurements (Martins *et al* 2020) and synthetic PIV using tracer particles with different diameters seeded through the jet and pilot regions, and (b) associated errors.

flow by seeding the jet only under similar conditions to those of the present work, among a variety of other non-combusting and combusting conditions. Although additional measurements employing a hot-wire anemometry, which is a particle-free point-wise velocimetry, have also been carried out by these authors, the hot-wire measurements are not reproduced here because the stationary single-wire system used cannot distinguish velocity components and it is prone to rectification, drop-out and cross-flow errors, as discussed by Panchapakesan and Lumley (1993). Corresponding errors between velocities from PIV and LES are presented in figure 5(b). The LES centreline velocity profile starts at zero, decreases towards a global minimum at $z/D_0 = 0.53$ with $V_z/V_0 = -0.29$, increases towards a global maximum at $z/D_0 = 2.87$ with $V_z/V_0 = 0.98$ and then monotonically decreases. The negative values are related to the inner recirculating region generated in annular jets (Ko and Chan 1979). At the bottom of this region ($0 \leqslant r/D_0 \lesssim 2.3$ and $z/D_0 \lesssim 1$) a strong recirculating toroidal vortex develops (Martins *et al* 2020). The maximum centreline velocity occurs when the jet potential core merges towards the nozzle axis upstream of the inner mixing region. The present centreline velocity asymptotes towards a decay proportional to z^{-1} for downstream positions $z/D_0 \gtrsim 5$. This decay trend is in concordance with vast literature (Panchapakesan and Lumley 1993, Boersma *et al* 1998, Pope 2000, Antoine *et al* 2001, Martins *et al* 2020). Excellent agreement is observed among the LES flow profile and those when small and medium particles are used, indicating that these sub-micron particles track the gas motion with fidelity. The greatest errors occur at $z/D_0 < 1.8$. Besides the aforementioned sources of error, this particular location is more influenced (due to the larger velocity gradients and smallest flow length scales) by spatial filtering imposed by the cross-correlation window employed in the velocity evaluation (Foucaut *et al* 2004, Li *et al* 2007, Atkinson *et al* 2014, Scharnowski and Kähler 2020) as well as the light sheet thickness (Atkinson *et al* 2014, Raffel *et al* 2018), both around $0.27\,D_0$. In the velocity profile from synthetic PIV using large particles, the averaged velocity peak is shifted approximately $1.7\,D_0$ further downstream compared to that of the standard LES profile. Therefore, the flow velocity is underestimated at the region $1.3 < z/D_0 < 4$ and it is overpredicted at $4.7 < z/D_0 < 16$. The observed velocity slip is caused by the particle inertia. The velocity slip behaviour was anticipated by analysing the Stokes number, which is much larger than the recommended limit of 0.1. The St of the largest tracer particles under the present study is two orders of magnitude greater than that of medium-sized particles, which tend to closely follow the flow. All investigated profiles collide on top of each other for axial positions above $16\,D_0$ (within variations below 2% of V_0), indicating that the particles accurately track the flow from this location onwards. This is a consequence of the increase of the characteristic time scale of the gas flow with the square of the axial distance from the jet exit, leading to a much lower Stokes numbers at these downstream locations. This effect, related to the jet spreading, is well-known and described in the literature (Pope 2000). While the LES profile of axial velocity compares well with that from PIV measurements (Martins *et al* 2020) for axial positions above $9\,D_0$, great discrepancies are observed for upstream locations. The LES employs a turbulent flow from a straight annular pipe as the jet inlet boundary (section 4), which seems to oversimplify the complex nozzle geometry leading to differences from the actual flow discharged through the nozzle of the SpraySyn burner, as discussed in Martins *et al* (2020). Despite the jet inlet discrepancies, normalized profiles of measurements and simulations by self-similar variables are alike within the developed region of the jet, as will be presented at the end of this section. Centreline profiles of time-averaged axial velocity from synthetic PIV seeding the jet only with small or medium particles show equivalent behaviour to those when pilot and jet streams are seeded together (differences of about 1% for positions above $6\,D_0$) and, therefore, are not plotted for sake of space.

Figure 6 presents radial profiles of time-averaged axial velocity at selected distances from the jet exit for the same

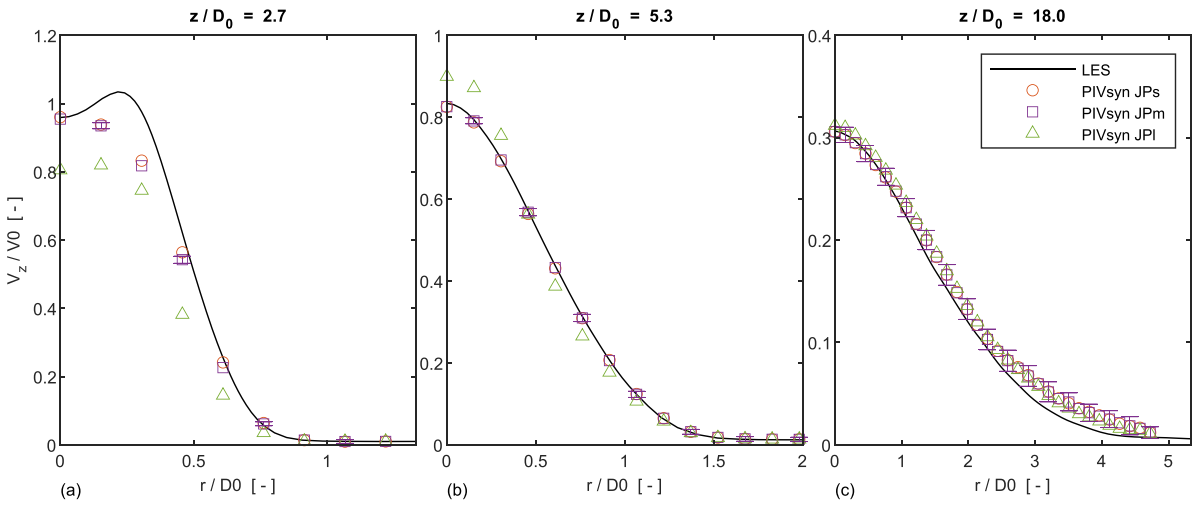

Figure 6. Radial profiles of (a) time-averaged axial velocity from standard LES and synthetic PIV using tracer particles with different diameters seeded through the jet and pilot regions together, and (b) corresponding errors.

seeding configurations of figure 5. Uncertainty bars for the medium-sized particle are included every second velocity point. Overall, the differences between profiles from small and medium particles are negligible. Velocities estimated from PIV are unable to detect the off-centred peak on the LES radial profile at $z/D_0 = 2.7$ (figure 6(a)), because of PIV spatial filtering as the interrogation window size of $0.26\,D_0$ is on the order of the slit width of the annular nozzle. In the case of large particles, the particle lag effect deteriorates even more the velocity estimate. Velocity values are underpredicted around the jet center at $z/D_0 = 2.7$ and overpredicted at $z/D_0 = 5.3$ (figure 6(b)). A third detrimental effect appears for axial positions above $6.7\,D_0$, where the jet and pilot streams are fully-merged. Upstream that location, the present flow behaves as a seeded combined jet surrounded by an unseeded sheath gas, roughly independent of the injection region of seeding particles. For this type of flow, a noticeable intermittency effect is present at the jet shear layer, where there is a pronounced mixing between seeded and unseeded gases. Figure 6(c) exemplifies the intermittency effect at $z/D_0 = 18$. Profiles of all particles are virtually the same considering the uncertainty levels. The intermittency causes a clear positive bias error on the nominal value of the velocity. The introduced bias error is of the order of the computed uncertainty.

To better understand the intermittency effect, radial profiles of time-averaged velocities at $z/D_0 = 5.3$ are analysed, since at this location, the axis of the jet core has already merged with the jet centreline and the pilot gas is still present around the jet flow. Figures 7(a) and 8(a) present radial profiles of axial and radial velocity components, respectively, estimated by synthetic PIV from medium-sized particles added through the jet only, the pilot gas only and through both regions. Radial profiles computed by LES are plotted for a gas flow reference. Uncertainty bars for the synthetic PIV evaluations with the jet only and the entire flow seeded are included every fourth velocity point. The corresponding velocity errors between the synthetic PIV evaluation using selective seeding (PIVsyn Jm and PIVsyn Pm) with that seeding both streams (PIVsyn JPm) are displayed in figures 7(b) and 8(b). From figures 7 and 8, the intermittency effect becomes obvious when selective seeding is adopted. Seeding the flow through the pilot gas only underestimates the axial and radial velocities at $0 \leqslant r/D_0 \lesssim 1$, corresponding to regions around the jet centre. On the other hand, seeding the flow through the jet gas only overestimates both velocity components at $0.7 \lesssim r/D_0 \lesssim 2$, positions around the shear layer. The latter bias is a consequence of the velocity evaluation from intermittent tracer particles (with inertia) that are spread or are convected by coherent structures from the high-momentum jet into the mixing region with entrained unseeded fluid from the low-momentum pilot gas. For the radial velocity when seeding exclusively the jet (figure 8(a)), only positive values are observed, indicating that the negative radial velocities at the jet boundaries due to entrainment cannot be captured. Different from the axial velocity, the bias error in the radial velocity (figure 8(b)) is still above the present uncertainty value at $r/D_0 = 2$, where the PIV evaluation ends due to the jet boundary. It is worth mentioning that PIV measurements of the time-averaged radial velocity are challenging because the values are usually less than 2% of the centreline axial velocity, therefore, close to the commonly reported uncertainty levels of the technique (Sciacchitano 2019). The nominal values of velocity computed by PIV with a seeded jet surrounded by an unseeded environment is always above those obtained with the entire flow seeded. This finding has been already perceived in different particle-based velocity measurement techniques by other researchers (Birch and Dodson 1980, Dibble *et al* 1987, Rice *et al* 2015). Overall, the lowest bias errors when only one region can be seeded occur for seeding through the pilot gas only (average bias error in the time-averaged axial velocity of about -3% in the present work), instead of the jet gas only (average bias error of about 9%). This somehow non-intuitive result is in agreement with the literature (Dibble *et al* 1987). When the entire flow is seeded, the intermittency effect vanishes and the synthetic PIV profile coincides with that obtained by LES. Identical results are observed for the small particles and are

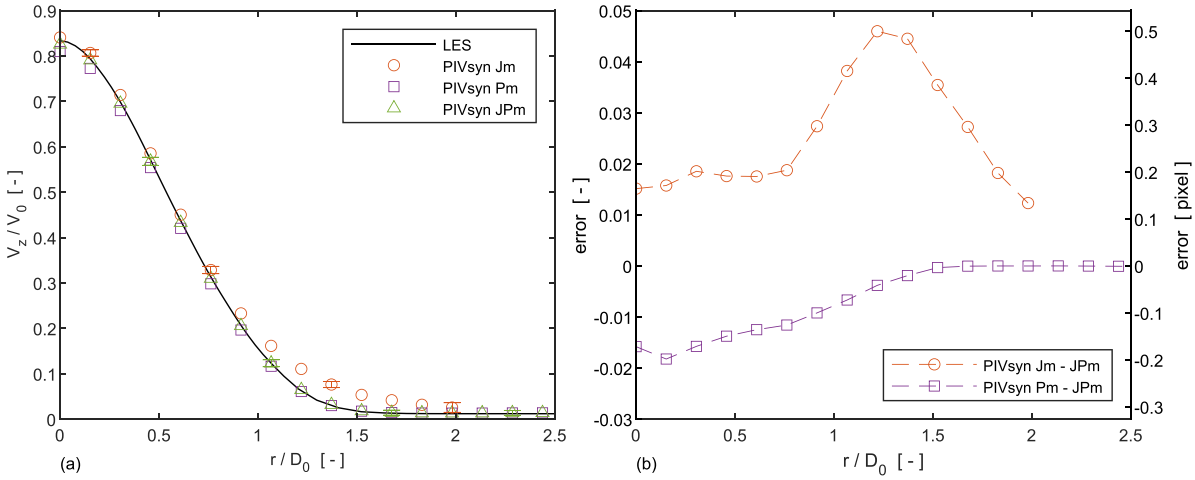

Figure 7. Radial profiles of (a) time-averaged axial velocity at $z/D_0 = 5.3$ from standard LES and synthetic PIV using tracer particles injected through the jet only, pilot only and both regions, and (b) corresponding errors.

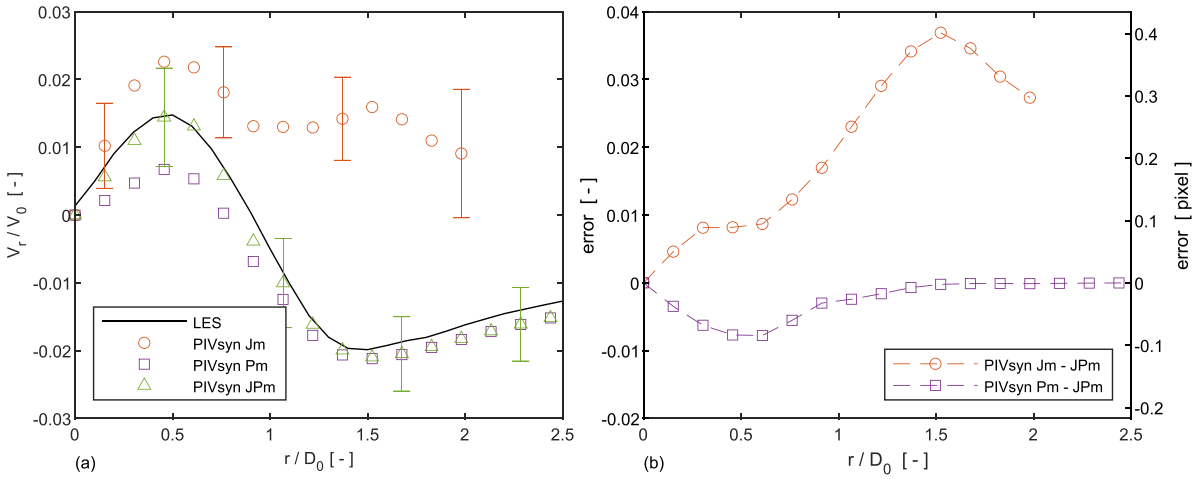

Figure 8. Radial profiles at $z/D_0 = 5.3$ of (a) time-averaged radial velocity from standard LES and synthetic PIV using tracer particles injected through the jet only, pilot only and both regions, and (b) associated errors.

not plotted for sake of space. For the large particles, the intermittency effect is combined with that of particle lag, increasing the bias errors and extending the limits of the aforementioned regions.

Figure 9 shows radial profiles of the Reynolds stress components within the *rz*-plane obtained by the synthetic PIV using different tracer particles added through the jet only, pilot only and both regions. These profiles are compared with those from the standard LES. Uncertainty bars are displayed every second point for the PIV evaluation with both regions seeded. The radial profiles of Reynolds stresses reflect the velocity fluctuations and the different levels of shear in the turbulent jet flow. In the jet shear layer region, large velocity gradients create off-centred peaks in all Reynolds stresses, while, at the jet centre, the velocity fluctuations are responsible for the large values in the Reynolds normal stresses (figures 9(a) and (b)).

The spatial filtering associated with the interrogation box region (equation (8)) of the present noiseless synthetic PIV has a small effect on the time-averaged velocity at $z/D_0 \gtrsim 5$. Nevertheless, noticeable bias errors due to filtering are observed when evaluating the Reynolds stress values of the simulated gas flow at $z/D_0 = 5.3$ by all synthetic PIV cases (figure 9). Since the average core diameter of intense vortical structures in turbulent flows is found to be about 10η (Elsinga and Marusic 2010), the interrogation window size and the light sheet thickness of a PIV experiment should be optimised to less than half of this length (Nyquist sampling theorem) in order to properly resolve the turbulent fluctuations. The Kolmogorov length scale of the present turbulent jet flow at $z/D_0 = 5.3$ computed by the LES σ-model (Nicoud *et al* 2011) is $\eta \approx 0.0085\, D_0$, leading to a relative window size of about 32 η and a light sheet thickness of around 36 η. Therefore, the oversized interrogation box region attenuates the Reynolds stress on average between -30% and -40% using suitable tracers (i.e. small and medium particles) at this axial location. The filtering in the Reynolds stress is worst for large particle tracers with greater Stokes numbers (green symbols in figure 9). The spatial filtering behaviour is in agreement with Atkinson *et al* (2014). They reported underestimated Reynolds stresses by as much as -50% when spatial filtering velocity

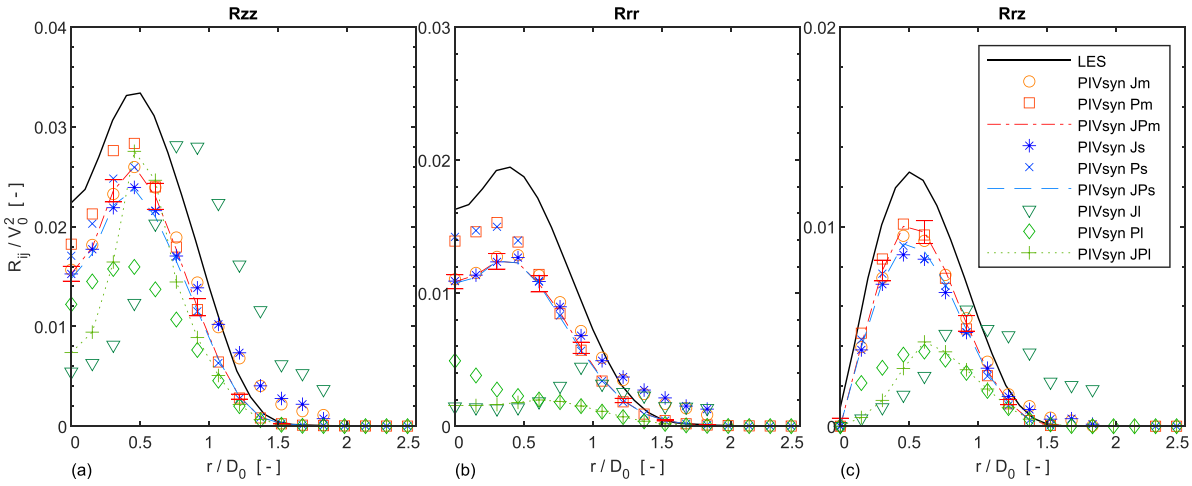

Figure 9. Radial profiles of the Reynolds normal stress along the (a) axial and (b) radial directions, and (c) Reynolds shear stress at $z/D_0 = 5.3$ from standard LES and synthetic PIV using small, medium and large seeds added through the jet only, pilot only and both regions. (For interpretation of the colour in this figure, the reader is referred to the web version of this article).

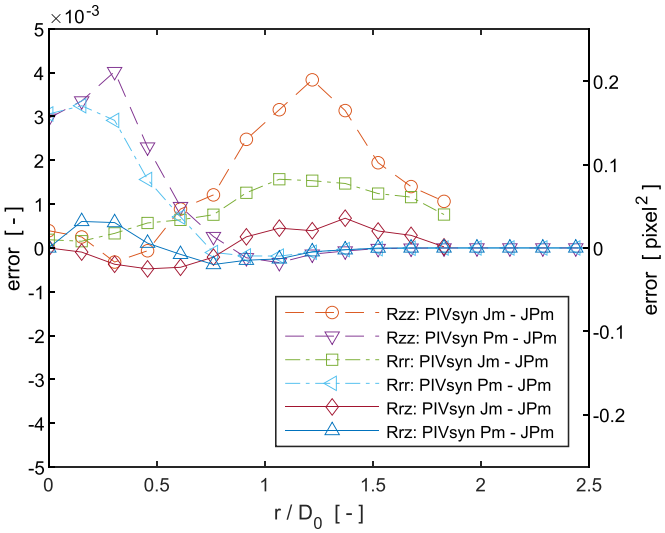

Figure 10. Radial profiles of bias errors in the Reynolds stress values at $z/D_0 = 5.3$ between synthetic PIV using medium particles injected through the jet only, pilot only and both regions.

fields obtained from direct numerical simulations of a turbulent boundary layer at typical interrogation box sizes used in PIV experiments. Interestingly, many PIV measurements without optimized window sizes found in the literature show lower attenuations of the expected Reynolds stress values than those reported here due to the intrinsic measurement noise that counterbalance the filtering effect (Foucaut *et al* 2004, Atkinson *et al* 2014). A comprehensive analysis of the bias error caused by the filtering effect is out of the scope of the present paper.

As the jet evolves, the Kolmogorov length scale along the centreline of the present turbulent jet simulation increases linearly with axial distance within the developed region. Therefore, the interrogation box at the top of the investigation domain becomes around the size of the intense vortical structures. The linear behaviour of the Kolmogorov length scale in turbulent jets is in agreement with the literature (Boersma *et al* 1998, Antoine *et al* 2001). The relative sizes of the 16-pixel interrogation window and the relative light thickness at $z/D_0 = 18$ are around two-fold smaller than those at $z/D_0 = 5.3$ with respect to the Kolmogorov scale. This leads to a less than -20% attenuation of the Reynolds stresses evaluated at $z/D_0 = 18$ by the synthetic PIV using medium-sized particles (as will be observed in figure 12).

The intermittency effect can be clearly recognized in figure 9 when comparing the radial profiles of the Reynolds stresses evaluated by synthetic PIV using particles with similar sizes seeded through different inlet regions. Figure 10 presents the errors between the Reynolds stress values evaluated using selective seeding with medium-sized particles only, for better visualization. For the investigated Reynolds stresses using small and medium-sized tracers, the values are overpredicted (on average between 10% and 20% considering the entire profile) at $0.7 \lesssim r/D_0 \lesssim 2$ when seeding the flow through the jet gas only and at $0 \leqslant r/D_0 \lesssim 0.7$ when seeding the flow through the pilot region only. The bias errors in the Reynolds stress values for the large seeding particles are much higher and the radial region extent where they occur are different due to a combined effect of intermittency and particle lag. The increase in the bias error for the second-order statistics due to intermittency compared to that reported for the time-averaged velocity has been previously recognized by other researchers (Birch and Dodson 1980, Rice *et al* 2015). Even larger bias errors are expected in combusting flows (higher instantaneous velocity gradients and density variations) and for derived flow quantities such as turbulent fluxes and velocity gradients. Nevertheless, future investigation is necessary to confirm these expectations.

Our attention is now turned to the self-similar behaviour of the jet. For the present turbulent annular jet weakly confined by a coflow, a self-similar behaviour of the radial profiles of the time-averaged velocity is already observed for positions above $5\,D_0$ (with normalized root-mean-square deviations below 2%), which is closer to the jet exit compared to turbulent

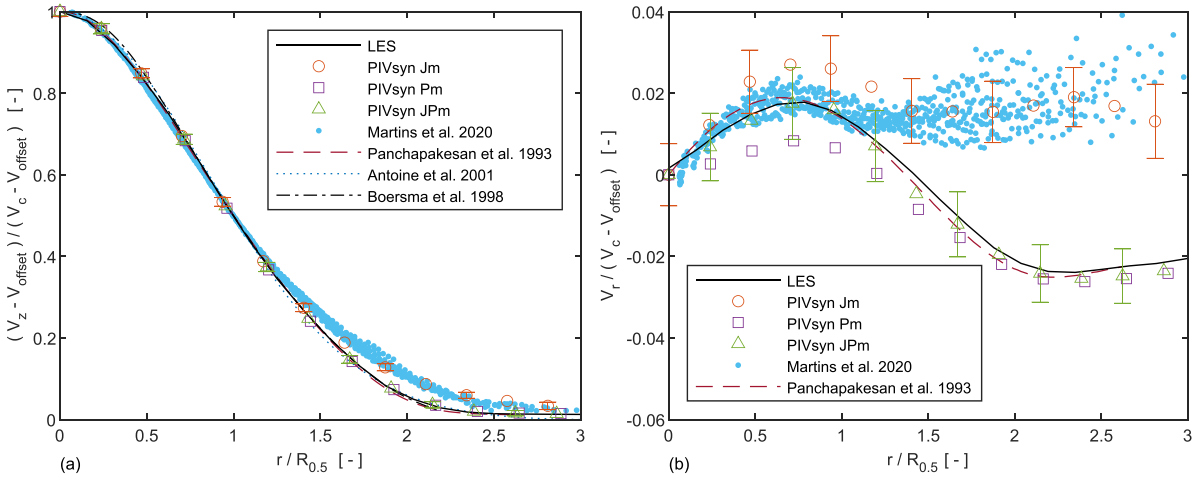

Figure 11. Self-similar radial profiles of time-averaged (a) axial and (b) radial velocity components from standard LES, synthetic PIV with medium-sized particle tracers and literature data (Panchapakesan and Lumley 1993, Boersma *et al* 1998, Antoine *et al* 2001, Martins *et al* 2020).

jets without coflow (Martins *et al* 2020). The radial profiles become self-similar when the velocity is normalized by the local centreline velocity V_c, corrected by the velocity offset V_{offset} due to the coflow (Antoine *et al* 2001), and the radial coordinate is normalized by the local half-velocity width $R_{0.5}$, following Pope (2000). The velocity offset can be determined based on the averaged streamwise velocity at the outermost annular region. Figure 11 shows self-similar radial profiles at $z/D_0 = 5.3$ of time-averaged axial and radial velocity obtained by standard LES and synthetic PIV using medium-sized tracer particles, as well as measurements and numerical simulations from the literature (Panchapakesan and Lumley 1993, Boersma *et al* 1998, Antoine *et al* 2001, Martins *et al* 2020). Uncertainty bars are added only on every second velocity location of the synthetic PIV seeding through the jet only and both regions in order to not overcrowd the graph. Panchapakesan and Lumley (1993) measured velocity statistics of a turbulent round free jet by a x-probe hot-wire anemometer mounted on a moving shuttle, Boersma *et al* (1998) performed a direct numerical simulation (DNS) of a low-turbulent round free jet, Antoine *et al* (2001) reported statistics of a turbulent round jet discharging into a co-flowing stream using laser-induced fluorescence combined with 2D laser Doppler velocimetry with the entire flow seeded with tracer particles, while Martins *et al* (2020) measured the PIV velocity of a seeded turbulent jet issued through the SpraySyn-burner nozzle weakly confined by unseeded co-flowing streams under the same flow conditions simulated here. The velocity offset values used for normalization are zero for Panchapakesan and Lumley (1993) and Boersma *et al* (1998), 0.5 m s^{-1} for Antoine *et al* (2001), and 0.15 m s^{-1} for the standard LES, synthetic PIV and Martins *et al* (2020). The measurements performed by Martins *et al* (2020) have the potential to suffer from intermittency effect in the mixing region due to the selective seeding of the jet only, whereas the other measurements and DNS from the literature are expected to well represent the true velocity profiles. Indeed, from figure 11, excellent agreement is obtained among the corresponding measured and simulated self-similar radial profiles of axial and radial velocities, confirming the expected bias behaviour. The bias error due to intermittency for selectively seeding the jet only (PIVsyn Jm and Martins *et al* 2020) is evident between $1.5 \lesssim r/R_{0.5} \lesssim 2.5$ for the axial velocity, reaching a maximum of about 5% of the centreline velocity at $r/R_{0.5} \approx 2$ (jet shear layer). The bias error trend in the radial profile of time-averaged axial velocity is in agreement with other researchers (Birch and Dodson 1980, Dibble *et al* 1987). For the radial velocity component (figure 11(b)), the bias error due to seeding the jet only is visible at further radial locations ($r/R_{0.5} \gtrsim 1$). It is interesting to note that, due to the normalization by the local centreline velocity of each selective seeding case (which is overestimated by approximately 2% for the seeded jet and underestimated by the same amount for the seeded pilot), the relative bias errors are slightly reduced compared to those reported in figure 7.

For the present turbulent annular jet surrounded by co-flowing streams, self-similar radial profiles of the Reynolds stresses are found for axial positions above $30\,D_0$, considering normalized root-mean-square deviations up to 15% (Martins *et al* 2020). Figure 12 compares radial profiles of Reynolds stresses normalized by self-similar variables from the present LES and synthetic PIV seeding the jet only with medium particles at $z/D_0 = 18$ (the furthest axial position still reliable) with those from the literature (Panchapakesan and Lumley 1993, Boersma *et al* 1998, Antoine *et al* 2001, Martins *et al* 2020). Although the normalized profiles from the LES and synthetic PIV at $z/D_0 = 18$ are not yet fully converged towards self-similar profiles due to the insufficient distance from the jet exit, profiles at further downstream positions are not trustworthy because they can be influenced by the close-by outlet boundary of the simulated domain. For better visualization, synthetic PIV curves when seeding the pilot only or the pilot and jet regions concomitantly are not plotted because they are indistinguishable due to the fully merged jet and pilot flows at this location, as discussed previously (figure 2). The normalized profiles of Reynolds stresses from the PIV measurements performed by our group under similar conditions (Martins *et al* 2020) are taken around $20\,D_0$ above the jet exit, because it is the closest axial position compared to the present profiles from

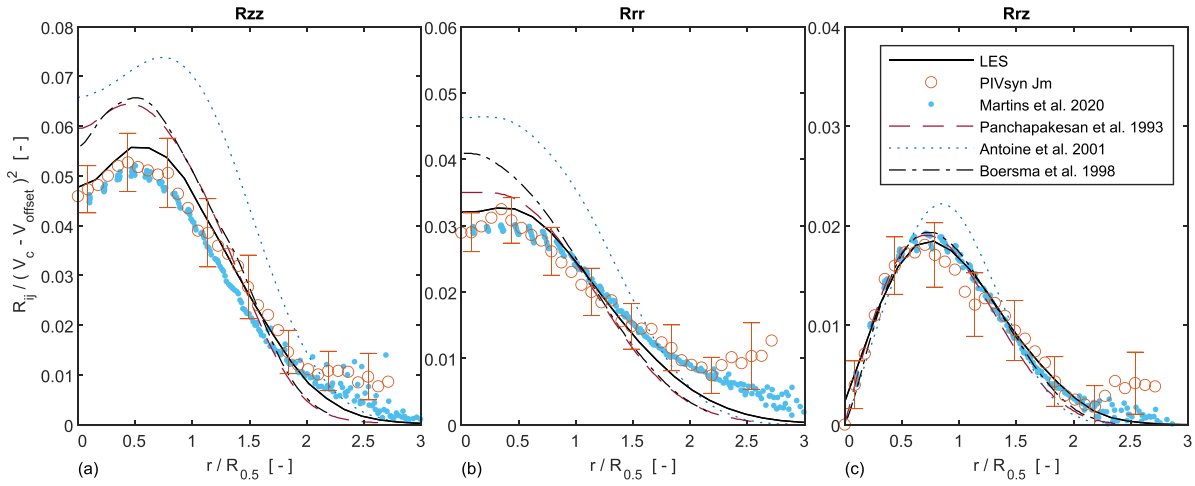

Figure 12. Radial profiles of the Reynolds normal stress along the (a) axial and (b) radial directions, and (c) Reynolds shear stress normalized by self-similar variables from standard LES, synthetic PIV with medium-sized particle tracers at $z/D_0 = 18$ and from literature data (Panchapakesan and Lumley 1993, Boersma *et al* 1998, Antoine *et al* 2001, Martins *et al* 2020).

the simulations. The normalized profiles of Reynolds stresses computed from the synthetic PIV capture the intermittency behaviour resulting from selective seeding measurements, as can be observed by the excellent agreement with the profiles from PIV measurements (Martins *et al* 2020). The synthetic PIV data detaches from the measurements for $r/R_{0.5} > 2$ due to the lower amount of independent vectors for converged statistics. The effective number of vectors drops drastically to less than one hundred at these locations, due to mainly the increase of the characteristic time scale of the flow and the border oscillation of the seeded jet flow (as discussed in section 4.4). It is important to mention that other differences between corresponding normalized PIV profiles from simulation and measurement may exist because the latter profile is at a further downstream position but still not in the self-similar region.

The Reynolds stress self-similar profiles are not expected to be identical for different jets, contrarily from the time-averaged self-similar profiles, because the former profiles strongly depend on the initial conditions, boundaries and flow history of each jet (George 1989, Boersma *et al* 1998, Martins *et al* 2020). That explains the amplitude differences observed among corresponding Reynolds stress profiles from the two round free jets (Panchapakesan and Lumley 1993, Boersma *et al* 1998), round jet with coflow (Antoine *et al* 2001) and the annular jet issued through the SpraySyn burner (present work and Martins *et al* 2020).

The agreement between simulation and experiment validates our biased synthetic PIV in the self-similar region (figures 11 and 12) and allows for assessing corresponding unbiased profiles from the standard LES simulation. Generally speaking, unbiased statistics can be estimated using biased numerical simulations that match corresponding biased measurements if those simulations are capable of emulating the physics causing the bias effect on the measurements. Then, unbiased corresponding statistics can be determined within the matched domain. Here we demonstrate the approach to the radial profiles of time-averaged velocities and Reynolds stresses normalized by self-similar variables. In principle, the approach can be extended, for example, for non-normalized higher-order flow statistics in the entire 3D field if corresponding statistics of interest are converged and agree with those from the experiments. But further investigation in different types of flows is required to corroborate this hypothesis. It is important to stress that the extrapolation of the simulated data beyond the measurement domain employed for validation as well as using the simulation to assess other flow quantities not validated by measurements might deviate from the true flow. The present approach can be potentially employed in other geometries and flows, observing the applicability limits.

Additionally to the aforementioned mitigation approach, the bias error due to particle lag and intermittent particle seeding might be attenuated in non-optimum measurements using adaptive PIV algorithms (e.g. Lindken *et al* 2003, Theunissen *et al* 2006, 2010, Yu and Xu 2016) or post-processing correction of statistics (e.g. Dibble *et al* 1987). In the adaptive PIV algorithms, the spatial locations of cross-correlation windows, their size, their shape and the location of the computed velocity vector can be optimised based on the image seeding density and flow conditions; whilst, in the post-processing correction, profiles can be transformed based on conditional probability distributions of tracer particle sampling, for example. Nevertheless, further investigation is needed to confirm the advocated enhancement in the measurements using such methods. Besides particle-based techniques, other velocimetry approaches that do not rely on tracers might be an alternative to suppress the intermittency effect, such as hot-wire anemometer (e.g. Panchapakesan and Lumley 1993) and filtered Rayleigh scattering (Miles and Lempert 1990, Forkey *et al* 1996, Doll *et al* 2017).

6. Conclusions

Temporal and spatial inhomogeneity of the image seeding density can lead to the effect of intermittent particle seeding

due to turbulent mixing of fluids with different particle concentrations and characteristic velocities. The effect is related to the local evaluation of velocity from tracer particles with inertia that are convected from locations with different velocities than those at the measuring region, such as in strong vortices, vicinity of walls, shocks, flame fronts and mixing regions of selective seeding. The latter and its influence in the PIV bias error is critically reported in the present work for the case of a turbulent annular gaseous jet surrounded by low-momentum co-flowing streams dispersed through a standard burner (SpraySyn burner) under non-reacting environment. The discussion of the intermittency effect and its difference from particle lag is performed based on the time-averaged velocities and Reynolds stresses from standard LES and from synthetic PIV employing tracer particles with diameters of 0.037, 0.37 and 3.7 μm inserted into the flow through the jet only, the pilot gas only and through both regions. The main conclusions are summarized as follows.

- The well-known selection of tracer particles based on the Stokes number below 0.1 is the first rule to be observed. Particles with sub-micron size are appropriate as tracers in the present jet flow and tend to accurately follow the local fluid flow at homogeneous seeding density regions, corroborating previous research studies. This particle size is recommended when measuring gaseous flows with great velocities or accelerations. The use of particles with few-micron diameter incurs in negative and positive bias errors in the present velocity statistics, and leads to an offset of the axial velocity peak in the centreline profile, due to particle lag.
- In the mixing seeded-unseeded regions when selective seeding is employed, bias error in the fluid velocity towards the tracer particle velocity occurs. The LES using tiny sub-micron-size particles with low inertia (greatly fulfilling Stokes-number criterion) seeded through the jet only leads to higher averaged velocities than those of the gaseous flow in the inner mixing region and around the jet boundary layer, due to intermittency. In the developed jet region, when only the turbulent jet gas is seeded, the bias errors are generally insignificant in the jet centre, and increase towards the jet shear layer. On the other hand, when only the co-flowing low-momentum stream is seeded, the bias errors increase in the jet centre and become insignificant away from the centre.
- Self-similar radial profiles of velocity statistics are used to demonstrate that actual carefully-performed PIV measurements of a seeded turbulent jet issuing into unseeded co-flowing streams using sub-micron particles (Martins *et al* 2020) are biased at the jet shear layer. In their PIV measurements, the bias error is of the order of the computed uncertainty for the time-averaged axial velocity and Reynolds stresses, and it is much higher for the time-averaged radial velocity.
- Global seeding is always recommended with similar particle number density in all streams. When this is not possible, selective seeding of flow regions should be employed after a sensibility study of the velocity bias error. For the present LES case of a high-momentum jet weakly confined by a low-momentum stream, the selective seeding of the co-flowing stream only can lead to smaller bias errors in the radial profiles of time-averaged axial velocity at the jet boundaries than seeding the jet only in the developed jet region.
- Particle lag and intermittent particle seeding yield local averaged velocities that are not equal to the true averaged velocity of the fluid flow. The discrepancies can be higher in combusting flows and for derived flow quantities, such as Reynolds stresses, turbulent fluxes, and velocity gradients. When these effects can not be avoided (i.e. by suitable selection of tracer particles, homogeneous seeding density, appropriate evaluation algorithm and post-processing), the uncertainty associated with the bias error must be taken into account for the analyses, in particular for a fair comparison of measured data with numerical simulations.
- As a general rule, unbiased statistics can be assessed from biased numerical simulations that model the physics generating the bias effect on the measurements. In the present work, the approach is demonstrated for a PIV evaluation of a seeded turbulent annular gaseous jet surrounded by unseeded co-flowing streams. In this case, if the measured PIV velocity biased due to selective seeding of the jet only is reliably reproduced by the numerical simulations of the tracer particles, the unbiased corresponding velocity statistics can be estimated from the simulated gaseous flow. This condition is satisfied here for radial profiles normalized by self-similar variables, so unbiased time-averaged velocities and Reynolds stresses are retrieved from biased particle-based LES, which is confirmed comparing the biased and unbiased profiles with the literature. The approach may potentially be used to other flows and geometries, alleviating the bias effects.

Data availability statement

The data that support the findings of this study are available upon reasonable request from the authors.

Acknowledgment

The authors gratefully acknowledge the funding from the German Research Foundation (DFG) within the priority program SPP1980—'Nanoparticle Synthesis in Spray Flames SpraySyn: Measurement, Simulation, Processes' (BE 3773/3 and KR 3684/12).

ORCID iDs

Fabio J W A Martins https://orcid.org/0000-0002-5841-4228
Jonas Kirchmann https://orcid.org/0000-0001-8122-2577
Andreas Kronenburg https://orcid.org/0000-0002-7967-9567
Frank Beyrau https://orcid.org/0000-0002-8043-7194

References

Adrian R J 1991 Particle-imaging techniques for experimental fluid mechanics *Annu. Rev. Fluid Mech.* **23** 261–304

Antoine Y, Lemoine F and Lebouché M 2001 Turbulent transport of a passive scalar in a round jet discharging into a co-flowing stream *Eur. J. Mech.* B **20** 275–301

Atkinson C, Buchmann N A, Amili O and Soria J 2014 On the appropriate filtering of PIV measurements of turbulent shear flows *Exp. Fluids* **55** 1654

Battista F, Picano F, Troiani G and Casciola C M 2011 Intermittent features of inertial particle distributions in turbulent premixed flames *Phys. Fluids* **23** 123304

Bergthorson J M and Dimotakis P E 2006 Particle velocimetry in high-gradient/high-curvature flows *Exp. Fluids* **41** 255–63

Birch A D and Dodson M G 1980 Some aspects of velocity biasing in turbulent mixing flows resulting from non-uniform seeding *Opt. Acta* **27** 3–8

Boersma B J, Brethouwer G and Nieuwstadt F T M 1998 A numerical investigation on the effect of the inflow conditions on the self-similar region of a round jet *Phys. Fluids* **10** 899–909

Dibble R W, Hartmann V, Schefer R W and Kollmann W 1987 Conditional sampling of velocity and scalars in turbulent flames using simultaneous LDV-Raman scattering *Exp. Fluids* **5** 103–13

Doll U, Stockhausen G and Willert C 2017 Pressure, temperature and three-component velocity fields by filtered rayleigh scattering velocimetry *Opt. Lett.* **42** 3773–6

Elsinga G E and Marusic I 2010 Universal aspects of small-scale motions in turbulence *J. Fluid Mech.* **662** 20

Forkey J N, Finkelstein N D, Lempert W R and Miles R B 1996 Demonstration and characterization of filtered rayleigh scattering for planar velocity measurements *AIAA J.* **34** 442–8

Foucaut J-M, Carlier J and Stanislas M 2004 PIV optimization for the study of turbulent flow using spectral analysis *Meas. Sci. Technol.* **15** 1046

Fuchs W, Nobach H and Tropea C 1994 Laser doppler anemometry data simulation-application to investigate the accuracy of statistical estimators *AIAA J.* **32** 1883–9

Garcia D 2010 Robust smoothing of gridded data in one and higher dimensions with missing values *Comput. Stat. Data Anal.* **54** 1167–78

George W K 1989 The self-preservation of turbulent flows and its relation to initial conditions and coherent structures *Advances in Turbulence* (London: Taylor & Francis) pp 39–73

GUM 2008 Evaluation of measurement data—guide to the expression of uncertainty in measurement *Joint Committee for Guides in Metrology (JCGM 100:2008)*

Kähler C J, Scharnowski S and Cierpka C 2012 On the uncertainty of digital PIV and PTV near walls *Exp. Fluids* **52** 1641–56

Ko N W M and Chan W T 1979 The inner regions of annular jets *J. Fluid Mech.* **93** 549–84

Ko N W M and Kwan A S H 1976 The initial region of subsonic coaxial jets *J. Fluid Mech.* **73** 305–32

Li D-X, Lin Q-S, Zhong Q and Wang X-K 2012 Bias errors induced by concentration gradient in sediment-laden flow measurement with PTV *J. Hydrodyn.* B **24** 668–74

Li D-X, Muste M and Wang X-K 2007 Quantification of the bias error induced by velocity gradients *Meas. Sci. Technol.* **19** 015402

Lindken R, Poelma C and Westerweel J 2003 Compensation for spatial effects for non-uniform seeding in PIV interrogation by signal relocation *Proc. 5th Int. Symp. on Particle Image Velocimetry* p 3302

Martins F J W A, Kirchmann J, Kronenburg A and Beyrau F 2020 Experimental investigation of axisymmetric, turbulent, annular jets discharged through the nozzle of the SPP1980 SpraySyn burner under isothermal and reacting conditions *Exp. Therm. Fluid Sci.* **114** 110052

McLaughlin D K and Tiederman W G 1973 Biasing correction for individual realization of laser anemometer measurements in turbulent flows *Phys. Fluids* **16** 2082–8

Melling A 1997 Tracer particles and seeding for particle image velocimetry *Meas. Sci. Technol.* **8** 1406

Menser J, Kluge S, Wiggers H, Dreier T and Schulz C 2014 Approach to standardize a spray-flame nanoparticle synthesis burner *Int. Workshop on Laser-Induced Incandescence (Hven, Sweden)*

Miles R and Lempert W 1990 Two-dimensional measurement of density, velocity and temperature in turbulent high-speed air flows by UV rayleigh scattering *Appl. Phys.* B **51** 1–7

Nicoud F, Toda H B, Cabrit O, Bose S and Lee J 2011 Using singular values to build a subgrid-scale model for large eddy simulations *Phys. Fluids* **23** 085106

Nobach H 2015 Corrections to the direct spectral estimation for laser doppler data *Exp. Fluids* **56** 109

Panchapakesan N R and Lumley J L 1993 Turbulence measurements in axisymmetric jets of air and helium. Part 1. Air jet *J. Fluid Mech.* **246** 197–223

Picano F, Battista F, Troiani G and Casciola C M 2011 Dynamics of PIV seeding particles in turbulent premixed flames *Exp. Fluids* **50** 75–88

Pope S B 2000 *Turbulent Flows* 1st edn (New York: Cambridge University Press)

Raffel M, Willert C E, Scarano F, Kähler C J, Wereley S T and Kompenhans J 2018 *Particle Image Velocimetry* 3rd edn (Berlin: Springer)

Ragni D, Schrijer F, Van Oudheusden B W and Scarano F 2011 Particle tracer response across shocks measured by PIV *Exp. Fluids* **50** 53–64

Rice B E, Goyne C P and McDaniel J C 2015 Seeding bias in particle image velocimetry applied to dual-mode scramjet *J. Propuls. Power* **31** 1393–403

Samimy M and Lele S K 1991 Motion of particles with inertia in a compressible free shear layer *Phys. Fluids* A **3** 1915–23

Samimy M and Wernet M 2000 Review of planar multiple-component velocimetry in high-speed flows *AIAA J.* **38** 553–74

Santiago J G, Wereley S T, Meinhart C D, Beebe D J and Adrian R J 1998 A particle image velocimetry system for microfluidics *Exp. Fluids* **25** 316–9

Scarano F and Riethmuller M L 2000 Advances in iterative multigrid PIV image processing *Exp. Fluids* **29** S051–60

Scharnowski S and Kähler C J 2020 Particle image velocimetry-classical operating rules from today's perspective *Opt. Lasers Eng.* **135** 106185

Schneider F, Suleiman S, Menser J, Borukhovich E, Wlokas I, Kempf A, Wiggers H and Schulz C 2019 SpraySyn—a standardized burner configuration for nanoparticle synthesis in spray flames *Rev. Sci. Instrum.* **90** 085108

Schulz C, Dreier T, Fikri M and Wiggers H 2018 Gas-phase synthesis of functional nanomaterials: challenges to kinetics, diagnostics and process development *Proc. Combust. Inst.* **37** 83–108

Sciacchitano A 2019 Uncertainty quantification in particle image velocimetry *Meas. Sci. Technol.* **30** 092001

Sciacchitano A and Wieneke B 2016 PIV uncertainty propagation *Meas. Sci. Technol.* **27** 084006

Smith M 1998 Application of a planar doppler velocimetry system to a high Reynolds number compressible jet *36th AIAA Aerospace Sciences Meeting and Exhibit* p 428

Stanislas M, Okamoto K and Kähler C 2003 Main results of the first international PIV challenge *Meas. Sci. Technol.* **14** R63

Stella A, Guj G, Kompenhans J, Raffel M and Richard H 2001 Application of particle image velocimetry to combusting flows: design considerations and uncertainty assessment *Exp. Fluids* **30** 167–80

Strobel R and Pratsinis S E 2007 Flame aerosol synthesis of smart nanostructured materials *J. Mater. Chem.* **17** 4743–56

Sung C J, Law C K and Axelbaum R L 1994 Thermophoretic effects on seeding particles in LDV measurements of flames *Combust. Sci. Technol.* **99** 119–32

Theunissen R, Scarano F and Riethmuller M L 2006 An adaptive sampling and windowing interrogation method in PIV *Meas. Sci. Technol.* **18** 275

Theunissen R, Scarano F and Riethmuller M L 2010 Spatially adaptive PIV interrogation based on data ensemble *Exp. Fluids* **48** 875–87

Thielicke W 2021 PIVlab—particle image velocimetry (PIV) tool with GUI *GitHub* (available at: https://github.com/Shrediquette/PIVlab/releases/tag/2.40) (retrieved 22 February 2021)

Thielicke W and Stamhuis E 2014 PIVlab—towards user-friendly, affordable and accurate digital particle image velocimetry in MATLAB *J. Open Res. Softw.* **2** 1

Thurow B S, Jiang N, Kim J-H, Lempert W and Samimy M 2008 Issues with measurements of the convective velocity of large-scale structures in the compressible shear layer of a free jet *Phys. Fluids* **20** 066101

Weller H G, Tabor G, Jasak H and Fureby C 1998 A tensorial approach to computational continuum mechanics using object-oriented techniques *Comput. Phys.* **12** 620–31

Wernet M P 2000 Development of digital particle imaging velocimetry for use in turbomachinery *Exp. Fluids* **28** 97–115

Westerweel J and Scarano F 2005 Universal outlier detection for PIV data *Exp. Fluids* **39** 1096–100

Willert C E and Gharib M 1991 Digital particle image velocimetry *Exp. Fluids* **10** 181–93

Williams O J H, Nguyen T, Schreyer A-M and Smits A J 2015 Particle response analysis for particle image velocimetry in supersonic flows *Phys. Fluids* **27** 076101

Yu K and Xu J 2016 Adaptive PIV algorithm based on seeding density and velocity information *Flow Meas. Instrum.* **51** 21–9